International Journal of Marine Energy 16 (2016) 298–316

Contents lists available at ScienceDirect

International Journal of Marine Energy

journal homepage: www.elsevier.com/locate/ijome

Experimental validation of the distributed drag method for simulating large marine current turbine arrays using porous fences

D.S. Coles *, L.S. Blunden, A.S. Bahaj

Energy and Climate Change Division, Sustainable Energy Research Group, Faculty of Engineering and the Environment, University of Southampton, UK[1]

ARTICLE INFO

Article history:
Received 31 May 2016
Revised 7 July 2016
Accepted 10 October 2016
Available online 11 October 2016

Keywords:
Large arrays
Porous fence
Distributed drag method
Array density
Bed drag
Regional scale modelling

ABSTRACT

Marine current energy conversion can provide significant electrical power from resource-rich sites. However since no large marine current turbine arrays currently exist, validation of methods for simulating energy extraction relies upon scaled down laboratory experiments. We present results from an experiment using porous fences spanning the width of a recirculating flume to simulate flow through large, regular, multi-row marine current turbine arrays. Measurements of fence drag, free surface elevation drop and velocity distribution were obtained to validate a method for parameterising array drag in the distributed drag approach, which is typically implemented in regional scale models. The effect of array density was also investigated by varying the spacing between fences. Two different inflow conditions were used; the first used the flume bed in its natural state, whilst the second used roughness strips on the flume bed to significantly enhance ambient turbulence intensity to levels similar to those recorded at tidal sites. For realistic array densities (<0.07), a depth averaged formulation of effective array drag coefficient agreed within 10% of that derived from experimental results for both inflow conditions. The validity of the distributed drag approach was shown to be dependent on longitudinal row spacing between porous fences and ambient turbulence intensity, two features that determine the level of wake recovery downstream of each porous fence. Finally a force balance analysis quantified the change in bed drag as a result of the presence of porous fence arrays. Adding arrays to the flow gave an increase in bed drag coefficient of up to 95% which was 20% of the total added bed and array drag coefficient. Results have implications for regional scale hydrodynamic modelling, where array layout along with site specific characteristics such as turbulence intensity and bed profile determine the validity of the distributed drag approach for simulating energy extraction.

© 2016 The Authors. Published by Elsevier Ltd. This is an open access article under the CC BY license (http://creativecommons.org/licenses/by/4.0/).

1. Introduction

For marine current turbines to make a significant contribution to electricity generation, methods for simulating large arrays must be validated to build confidence in performance predictions. Only then will it be possible to justify array design

* Corresponding author.
E-mail address: d.coles@soton.ac.uk (D.S. Coles).
[1] www.energy.soton.ac.uk.

http://dx.doi.org/10.1016/j.ijome.2016.10.001
2214-1669/© 2016 The Authors. Published by Elsevier Ltd.
This is an open access article under the CC BY license (http://creativecommons.org/licenses/by/4.0/).

Nomenclature

A_i	flume inlet cross sectional area (m^2)
A_o	flume outlet cross sectional area (m^2)
A_s	swept area (m^2)
A_t	rotor area (m^2)
A_P	array plot area (m^2)
A_o	flume outlet cross sectional area (m^2)
C_b	bed drag coefficient
C_e	equivalent added array drag coefficient
C_t	fence drag coefficient
$C_{t,a}$	array drag coefficient
$\overline{F}_a$	depth averaged array force (N)
F_b	bed drag force (N)
F_f	porous fence drag force (N)
F_w	weight force (N)
g	acceleration due to gravity (m/s^2)
h_i	inlet depth (m)
h_o	outlet depth (m)
k	physical roughness height (m)
l_a	longitudinal porous fence array length (m)
l_f	porous fence row spacing (m)
l_z	porous fence height (m)
n	porous fence number
p	Pitch between roughness strips (m)
ρ	density of water (kg/m^3)
Re	reynolds number
Re_b	boundary reynolds number
τ_a	array shear stress (Pa)
θ	flume bed slope angle (°)
$\overline{U}$	depth averaged flow velocity (m/s)
$U_{f,n}$	flow velocity through fence n at fence centroid height (m/s)
$U_{0,f}$	upstream flow velocity at fence centroid height (m/s)
u_*	friction velocity (m/s)
$u'w'$	magnitude of the shear stress (m^2/s^2)
v	kinematic viscosity of water (m^2/s)
z_0	roughness length (m)
β	porosity
ε	Blockage ratio
λ	array density

decisions, such as the longitudinal row spacing required to simultaneously maximise energy extraction, minimise array footprint and prevent potential detrimental environmental impact at specific sites.

The task of modelling the performance of turbines in arrays is a multi-scale problem where blade, turbine, array, site and regional scales are needed to incorporate all relevant physical effects [1]. This work focuses on the distributed drag method for simulating large arrays in regional scale models. In this approach, a drag is applied uniformly over the array plot area A_p and individual turbines are not modelled, allowing arrays to be simulated at acceptable computational expense. Assuming mesh independence for energy extraction is achieved, no further mesh preparation is required, meaning the same mesh can be used to investigate array size, positioning and density λ (defined as the ratio of total swept area of turbines A_s to the array plot area A_p) rather than having to adapt the mesh for any change in array layout. This method is typically used in the early stage of resource assessment to quantify far field effects [2], optimise array shape [3], quantify array-array interaction [4], quantify sediment dynamics [5] and quantify energy extraction [4,6–12].

Since no full scale arrays currently exist, validation of methods for simulating energy extraction by large marine current turbine arrays relies upon scaled down laboratory experiments. To date these have mainly focused on single devices [13–15] and interactions between only a few devices [16,17], often with no consideration to modification of ambient flow properties such as turbulence intensity to values observed at tidal sites. For these reasons further experimental work is needed to validate large array models [18].

The performance of individual turbines in a large array is complicated by the co-existence of multiple superimposed wakes, ambient flow velocity and turbulence, wake added turbulence, local bathymetry, and the effect of the boundary layer,

limiting our ability to correctly predict the performance of individual turbines in a large array. This work addresses this problem experimentally by characterising the flow through arrays of porous fences, used to simulate the far wake effects downstream of densely packed rows of marine current turbines at laboratory scale.

The paper provides an overview of the distributed drag approach for simulating large arrays and highlights the potential sources of error (Section 2). The experimental setup is then presented, outlining the procedure taken to quantify array drag, free surface elevation, bed drag and flow distribution within arrays of varying density (Section 3). Characterisation of the two different ambient flows used for each array is presented along with the thrust and wake characteristics of a single fence in both flows (Section 4). Flow is then characterised through arrays of porous fences with varying array density, λ. Analysis of flume discharge, free surface elevation, flow and fence load was used to quantify the accuracy of distributed drag method in quantifying array drag by comparing experimental results with estimates from a depth averaged formulation. Finally the effect of arrays on flume bed drag was quantified using experimental measurements using the simple force balance presented in Fig. 1.

2. Regional scale modelling of large arrays

2.1. Distributed drag method

Observations from windfarms [19] and scaled down wind and tidal farm experiments [20–23] show that flow within large arrays with more than four rows exhibit equilibrium conditions, where the flow dynamics between each row repeat and the wake recovers to the same magnitude by the time it reaches the next row downstream. This creates an even distribution in drag amongst rows in the equilibrium region, allowing the windfarm to be modelled using a uniform drag distributed over the array area. In the case of windfarms, energy loss from devices, the ground and turbulent dissipation is replenished by vertical energy transport from the boundary layer above the farm, creating an energy balance [24]. In the case of marine current turbine arrays, the longitudinal pressure gradient driving the flow as a result of the dynamic head drop across the array ($F_i - F_o$) and the weight component (F_w) are in balance with the opposing drag from porous fences, $F_{f,n}$ where n is the number of porous fences and the bed, F_b. This is demonstrated in Fig. 1, which shows the control volume used for the experiments carried out in this work. The force balance is given by Eq. (1) where the first two terms give the hydrostatic force at the inlet and outlet of the flume respectively. A_i and A_o are cross sectional areas at the inlet and outlet respectively.

$$\int_{z=0}^{h_i} \rho g z dA_i - \int_{z=0}^{h_o} \rho g z dA_o + F_w sin\theta - F_b - \sum_{i=1}^{n} F_{f,i} = 0 \tag{1}$$

The distributed drag approach is well suited for modelling this equilibrium flow state as it assumes a spatially averaged balance between momentum input and drag forces. Individual turbines are not modelled and instead an effective array drag ($\sum_{i=1}^{n} F_i$) is applied uniformly over the whole array plot area.

Flow must transition to equilibrium conditions which for windfarms has been shown to take up to 3 rows [20]. This could potentially create an uneven drag distribution amongst fences in this region if the flow through fences 1, 2 and 3 is such that $U_1 \neq U_2 \neq U_3$ (shown in Section 4, Fig. 10b). This is quantified in this work using load cell measurements on each fence in arrays of varying density.

2.2. Definition of 'large' array

For this work, an array is defined as 'large' if it has more than three equally spaced rows to investigate equilibrium conditions as flow develops through each row. Assuming the lateral and longitudinal spacing between devices does not exceed realistic values for spatially efficient array development of approximately 5 and 20 diameters respectively, this also satisfies another definition where turbines no longer perform as isolated turbines due to influences of the array on the flow dynamics

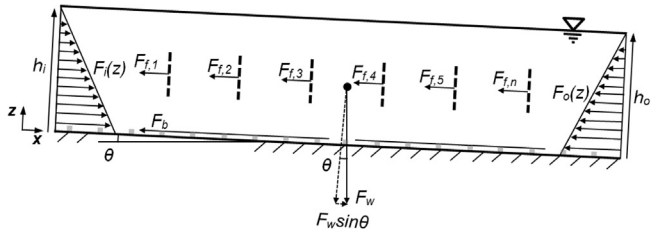

Fig. 1. Elevation view of recirculating flume experiment, showing the force balance between the hydrostatic forces F_i and F_o at inlet and outlet, the drag force from the flume bed, F_b, the weight component, $F_w sin\ \theta$ and the opposing force from each porous fence, $F_{f,n}$ where n is the number of porous fences. In the case of this experiment, bed slope angle, $\theta = 0.09°$, so is exaggerated for demonstrative purposes. Square grey blocks on the flume bed are roughness strips used to enhance ambient turbulence intensity and modify flow distribution in the vertical plane.

[25]. Furthermore, multi-row array layouts will enable significant levels of energy extraction to contribute towards power generation whilst respecting the spatial constraints at specific sites. This is of particular relevance at locations where other industries such as fishing and passenger ferries operate [26], as well as the potential environmental impact of large arrays such as enhanced levels of sediment transport depending on the proximity of turbines to sandbanks [27]. These considerations make it unlikely that single row arrays spanning the width of a channel can realistically be implemented, as has been considered in the past [4,6,10,28]. Finally, given that there is often an uneven spatial distribution in ambient kinetic energy flux over a site, such as has been shown for Alderney Race [29] for example, multi-row arrays will enable only the most energy dense plots to be developed to increase array performance. For these reasons there is a need to understand the flow dynamics through multi-row array layouts to estimate energy extraction and its environmental impact.

2.3. Parameterisation of effective array drag

The depth averaged force, $\overline{F_a}$ exerted on the flow by n turbines each with swept area A_t is given by [6,7,12,30]:

$$\overline{F_a} = \frac{1}{2}\rho \overline{U}^2 n A_t C_t \tag{2}$$

where $\overline{U}$ is the depth averaged flow velocity within the array and C_t is the thrust coefficient of a single turbine. Typically for marine current turbines the thrust coefficient used is $C_t = 0.8$ based on experiments of a scaled down device [14], which assume turbine thrust is a function of upstream hub height flow velocity, $U_{0,f}$. Depending on the vertical inflow distribution incident on a turbine or fence, it is conceivable that $\overline{U} \neq U_{0,f}$ as depth averaged models do not define the flow distribution in the vertical plane. If this is the case, the estimated turbine or fence drag using a depth averaged formulation (Eq. (2)) will be erroneous, given that C_t is derived from a hub height inflow. In a large array, where the slower moving wake from upstream turbines (or fences) impedes on downstream turbines, it is possible that $\overline{U} > U_{f,n}$ given that $\overline{U}$ is approximately constant throughout the array assuming the free surface slope is not significant. This is demonstrated in Fig. 2, which illustrates the vertical flow distribution of three flows all with the same depth averaged flow velocity $\overline{U}$. Each profile is based on results using Acoustic Doppler Anemometer (ADV) measurements taken upstream and within porous fence arrays in this work. The green profile shows a typical wake flow seen between fences in an array of porous fences.

The stress induced by the array over the array plot area, A_p is:

$$\tau_a = \frac{\overline{F}_a}{A_p} \tag{3}$$

This stress is added to the momentum equations in the form $\frac{\tau_a}{\rho h}$ where h is the flow depth, giving an extra depth averaged source term:

$$\frac{\tau_a}{\rho h} = \frac{\lambda C_{t,a}}{2h}|\overline{U}|\overline{U} = \frac{C_e}{h}|\overline{U}|\overline{U} \tag{4}$$

where $C_{t,a}$ is the total array drag coefficient and C_e is the effective array drag coefficient:

$$C_e = \frac{1}{2}\lambda C_{t,a} \tag{5}$$

C_e is added to the bed drag coefficient C_b to give the 2D formulation of combined drag as a shear force:

$$\frac{\tau}{\rho h} = \left(\frac{C_e + C_b}{h}\right)|\overline{U}|\overline{U} \tag{6}$$

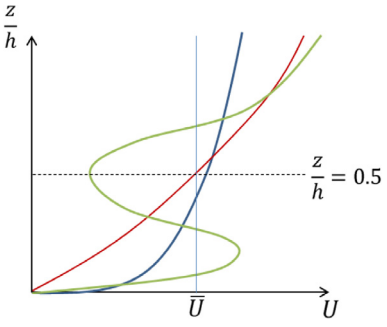

Fig. 2. Illustration of typical flow distribution in the vertical plane of three flows within an array of porous fences, all with the same depth averaged flow velocity, $\overline{U}$. Dotted horizontal line intercepts each flow profile at the centroid height of the fences, $z/h = 0.5$.

In most cases it is assumed that the presence of a marine current turbine array has no impact on the bed drag coefficient C_b. However for windfarm modelling different approaches have been taken, such as the assumption that bed drag increases due to flow diversion in the region under the turbines [31]. The change in bed drag will be quantified using the force balance described by Eq. (1).

The depth averaged array drag is estimated from Eq. (7), which will be compared with experimental values for array drag obtained from load cell measurements on each fence.

$$\overline{F}_a = \int\int_{A_p} \frac{1}{2}\rho C_e \overline{U}^2 dA \tag{7}$$

2.4. Summary of array drag parameterisation sources of error

In summary, doubts over the accuracy of the distributed drag approach for simulating large arrays arise from three main potential sources of error listed below:

I. The drag force of turbines exerted on the flow is parameterised based on the assumption that turbine thrust is dependent on upstream, hub height flow velocity, $U_{0,f}$. However in depth averaged formulations such as Eq. (2), turbine drag is estimated based on a depth averaged flow velocity $\overline{U}$. Depending on the flow distribution in the vertical plane, it is conceivable that $\overline{U} \neq U_{0,f}$, which would lead to an error in the estimated array drag. This discrepancy between $\overline{U}$ and $U_{0,f}$ will be made worse within an array where the drag of downstream fences are affected by the slower moving wake flow created by upstream fences. This can be quantified experimentally by measuring the thrust force on each fence using load cells with two different vertical inflow distributions, as outlined in Section 3.

II. In the transition region at the front of the array flow is developing to equilibrium conditions, creating an uneven drag distribution over the first few fences, which cannot be modelled by an evenly distributed drag. The consequence of this on the accuracy of the distributed drag approach was quantified for different array densities, again using load cell measurements on each fence.

III. The presence of an array could affect the bed drag coefficient, C_b in comparison with bed drag for ambient flow. This is quantified using a force balance (Eq. (1)) where the bed drag, F_b in the absence of turbines was compared with bed drag for flow through arrays of fences.

These sources of error are quantified experimentally to investigate the accuracy of an array drag parameterisation used in regional scale models. This array drag parameterisation was outlined above by Eqs. (2)–(6).

The effect of local blockage on the total array drag is another contributing source of error in the distributed drag method. However, it was not considered here as the effect of row blockage on fence thrust is taken into account directly through load cell measurements for each fence. Experimental analysis of the effect of local blockage on device thrust is covered in [32].

3. Experimental method

3.1. Experimental setup

A recirculating flume with 19 m working section, width $w = 1.37$ m and depth $h = 0.3$ m was used with porous fences positioned perpendicular to the flow (Figs. 3 and 4). The fences had height, $l_z = 0.1$ m and width $w = 1.34$ m and were placed at centroid height $z_h = 0.15$ m (mid depth, giving each fence a blockage ratio, $\varepsilon = 1/3$. The fences had 5×5 mm square perforations positioned at 8 mm centres, giving a porosity $\beta = 0.39$. A low porosity was chosen to ensure a significant change in free surface elevation across each porous fence array, flow velocity and thrust could be observed. Additionally, previous experiments using fences with higher porosity (greater open area) exhibited fence deformation when incident on high flow.

Roughness strips spanning the width of the flume were secured to the flume bed (shown in Fig. 4) to augment ambient turbulence intensities to levels representative of tidal flows. The geometry and spacing of the roughness strips was chosen based on results from large eddy simulations of turbulent flow over rib roughness [33]. In the literature different longitudinal roughness spacings (defined as the pitch p) and roughness heights k were investigated, where the reattachment length downstream of a roughness strip was shown to be a function of the pitch ratio p/k. It was found that for $p/k > 4$ (termed 'k-type' roughness), separation and reattachment occurs between roughness strips, causing larger eddies to emanate into the outer flow, enhancing ambient turbulence intensities. Greatest interaction between the flow in the roughness layer and the outer flow was achieved for a pitch ratio of $p/k = 10$. To ensure a significant increase in ambient turbulence intensity in this experiment, a pitch ratio of $p/k = 10$ was adopted here, where $p = 0.3$ m and $k = 0.03$ m.

Experiments were run with seven different arrays (Table 1). The first fence in each array was positioned at $x = 6$ m downstream of the flow straightener at the flume inlet. Fences were then positioned downstream at different spacings, l_f, with the last fence a distance l_a downstream of the first. Six spacings between fences were used at $l_f = 7l_z$, $10l_z$, $13l_z$, $16l_z$, $19l_z$ *and* $60l_z$.

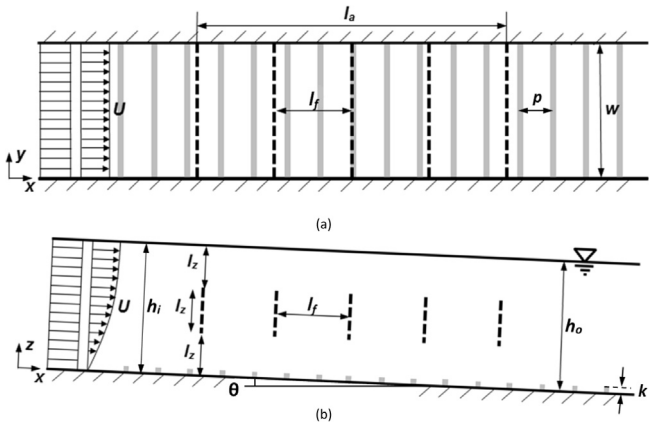

Fig. 3. Experimental setup showing (a) plan view and (b) elevation view of porous fences positioned in the recirculating flume with flow straighteners at the inlet and bed roughness attached to the flume bed shown by grey strips. In the case of this experiment, bed slope angle, $\theta = 0.09°$, so is exaggerated for demonstrative purposes.

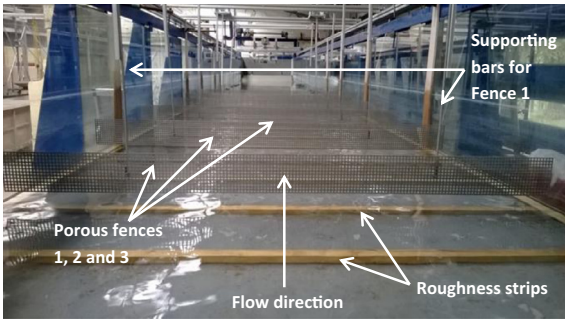

Fig. 4. Porous fences positioned in the flume with row spacing, $l_f = 7l_z$. Bed roughness positioned on the flume bed. Flume outlet with raised weir shown at the far end. Porous fences held in position using 2 thin vertical supporting bars.

Table 1
Characteristics of 7 different arrays used in the experiment.

Case	Array density, λ	No. fences	Spacing, l_f (l_z)	Array length, l_a (l_z)	Measurements
1	→0	1	–	–	Upstream mid depth flow velocity, $U_{0,hh}$, vertical flow velocity distribution within each array $U(x,z)$, flume discharge, Q, load on each fence, F_i, elevation drop across the array, Δz
2	0.033	2	60	60	
3	0.070	4	19	57	
4	0.078	5	16	64	
5	0.092	6	13	65	
6	0.117	7	10	60	
7	0.159	10	7	63	

This was seen as a sensible range to ensure varying degrees of interaction between fences and the wake of upstream fences so that this behaviour on the overall array drag could be investigated. The number of fences, n, was reduced with increasing row spacing, l_f, so that each array took up approximately the same plot area and length, l_a.

Initially the flume was run without porous fences to characterise the ambient flow, both with and without roughness strips secured to the flume bed. Centreline measurements of vertical flow distribution were obtained and the head drop between inlet and outlet was measured. Flow distribution was measured across the flume (along the y-axis) to quantify the boundary layer from the flume side walls.

Each fence was positioned in the flow using two narrow vertical bars (2 mm) connected 0.42 m from the centre of the fence. It was assumed these had no effect on the flow along the centreline of the flume where measurements were taken.

Initially results were obtained without the added roughness on the flume bed (referred to as Case A: without roughness from now on). Once results were obtained for all experiments listed in Table 1, the added bed roughness was secured to the bed and the experiments were repeated (referred to as Case B: with roughness from now on).

3.2. Measurements

A downward looking Acoustic Doppler Velocimeter (ADV) with 150 mm^3 sampling volume was used to measure the upstream velocity, $U_{0,f}$ at $x = 4$ m downstream of the flow straightener. The flume pump was adjusted to ensure a constant Froude number (based on $U_{0,f}$) of $Fr = 0.13$. This corresponds to an upstream mid-depth flow velocity at the centroid height of the fences, $U_{0,f} = 0.23$ m/s, giving a full scale tidal velocity of approximately 2.5 m/s and depth of 35 m by scaling flow velocity with channel Froude number. A sampling frequency of 200 Hz was used to capture turbulence properties of the flow. Flow velocity profiles and turbulence intensity profiles between fences were obtained using a sideways looking ADV along the centreline of the flume at $0.1l_z$, $0.3l_z$, $0.6l_z$, $0.9l_z$, $1.2l_z$, $1.5l_z$, $1.8l_z$, $2.2l_z$ and $2.7l_z$ above the flume bed. Three profiles between each fence were obtained, with the longitudinal spacing between profiles depending on the fence spacing, l_f. Profiles were obtained at $1l_z$ upstream of each fence (the closest the ADV could be positioned upstream of a fence), $3l_z$ downstream of each fence and one profile halfway in-between these positions to obtain the widest range in between fences.

Two load cells positioned 0.355 m either side of the centreline of each fence were used to measure the reaction on the supporting structure of each fence. An ultrasonic distance sensor (Senix Toughsonic TSPC-30 series) was used to measure flow depth along the centreline of the flume. With prior knowledge of the flume bed level, which drops almost linearly from inlet to outlet by 25 mm, the free surface elevation drop across each array was obtained. A discharge meter (Sonteq IQ Plus) positioned at the flume outlet measured discharge for each case. Measurements were used alongside flow depths to obtain depth averaged flow velocities.

3.3. Porous fences

At laboratory scale static porous disks/fences have been shown to reproduce the axial velocity flow field in the far wake (distances greater than approximately 5 diameters) downstream of a rotor [34] when the thrust coefficient of the disk is matched to the turbine it is simulating. Porous disks/fences dissipate energy in the wake through turbulence generation. No mechanical energy is extracted from the flow as with real turbines, so the energy contained in the near wake will be different. Additionally there is no turbine rotation which causes vortex sheets to shed from the trailing edge of the rotor blades and blade tips, generating blade vortices, however this phenomenon is also confined to the near wake region. Therefore porous fences have been chosen as a suitable method to simulate the far wake effects of turbines in large arrays, with a minimum spacing between rows of 7 diameters.

In [35] experiments were conducted to characterise jet flow through porous fences with porosity, $\beta = 0.41$, 0.5, 0.57 and 0.65. The jet flow velocity $U_0 = 40$ m/s and jet width, b_0 gave a jet Reynolds number of approximately 15,000. It was expressed that if the porosity scale is small relative to the jet scale, the flow through the fence should be independent of the details of the porosity (e.g. hole width/shape) and only on the value of porosity itself. Given that w_f is only 5% of fence height l_z, and less than 2% of the flow depth h, it was assumed that only the porosity itself was a significant parameter in determining the wake flow, not the porous geometry, however this was not investigated further. Using fence height l_z as the characteristic length scale gives a Reynolds number of 17,600. Alternatively, using the width of the square holes in each fence $w_f = 0.5$ cm as the characteristic length scale gives a Reynolds number of 900.

4. Results and discussion

4.1. Ambient flow characterisation

Fig. 5a shows data obtained experimentally of the ambient centreline vertical flow distribution using Case A: without roughness and Case B: with roughness, plotted alongside the depth averaged flow in each case. Flow using Case A: without roughness exhibits a logarithmic boundary layer in the bottom half of the water column up to approximately $z/h = 0.6$ above the bed, where all flow data points fit within 10% of a logarithmic distribution (Fig. 5b) with roughness length, $z_0 = 0.0002$ m. Based on results in [36] this is equivalent to a bed similar to sand/broken shell ($z_0 = 0.0003$ m). Flow distribution in the vertical plane compares well with flow data obtained in the Irish Sea [37], where ship mounted ADCP measurements in depths of approximately 50 m show a logarithmic profile in the lower 50–60% of the water column except at times of slack tide. Friction velocity was obtained from the gradient of the logarithmic flow distribution in the vertical plane, giving $u^* = 0.014$ m/s, agreeing within 7% of the friction velocity measured at Colvos Passage tidal site in Washington State, USA of 0.015 m/s [38]. The influence bed roughness has on the turbulent properties of the outer flow was determined using the roughness Reynolds number Re_r [39] (Eq. (8)).

$$Re_r = \frac{u_* k}{\nu} \tag{8}$$

where k is te physical roughness height and ν is the kinematic viscosity of water (1.3×10^{-6} m^2/s). For hydraulically rough flow separation occurs off the bed roughness geometry to directly influence the turbulent properties of the bulk flow, as is the case in real tidal flows. Based on $Re_r > 70$ for hydraulically rough flow, Case A: without roughness requires a minimum roughness, k_s = 6.5 mm assuming u^* = 0.014 m/s. Measurements of flume roughness were obtained using ultrasonic distance measurements, showing a 2 mm variation in bed surface elevation over multiple randomly selected regions of the flume, where typically this variation occurred over a 10 mm length, therefore it is unlikely that the flow is hydraulically rough using Case A: without roughness.

The fully developed vertical flow distribution using Case B: with roughness was quasi-steady, where at each roughness strip flow accelerates due to increased blockage and then slows in the cavity between each roughness strip, giving a variation in the flow profile (Fig. 5a). The friction velocity was estimated as u^* = 0.036 m/s, which is in close agreement with measurements in the Irish Sea of 0.031 m/s [37]. Fig. 5b shows the vertical distribution in flow is logarithmic above z/h = 0.1, where the flow is displaced vertically by the roughness a distance equal to the summation of the displacement height d and roughness length z_0 in the roughness sub layer [39]. The criteria for hydraulically rough flow is met easily for Case B: with roughness according to Eq. (8) given that k = 0.03 m in this case.

Fig. 5a shows that for both Case A: without roughness and Case B: with roughness, at $z/h \approx 0.4 \approx e^{-1}$ the depth averaged flow velocity $\overline{U}$ is equal to the mid-fence height ambient flow velocity $U_{0,f}$. It is interesting to note that this would be expected to be the case if the flow profile was logarithmic over most of the depth [32]. This is an important point when considering the validity of the distributed drag method for modelling large multi-row arrays. If we assume the row spacing is sufficient for wakes to recover completely before reaching the next downstream row, the numerical formulation for array drag described by Eq. (2) will underestimate array drag because $\overline{U} < U_{f,0}$. However if row spacing is insufficient for complete wake recovery to occur, this may indirectly improve Eq. (2)'s accuracy of array drag if the depth averaged flow $\overline{U}$ becomes a closer representation of the flow velocity at porous fence centroid height U_f. The depth averaged flow velocity recorded using Case A: without roughness was $\overline{U}$ = 0.215 m/s, 6% lower than the mid depth (z/h = 0.5) streamwise flow velocity, $U_{f,0}$ = 0.225 m/s. Similarly using Case B: with roughness, $\overline{U}$ was approximately 10% lower than $U_{f,0}$. Therefore the drag from the first fence, $F_{f,1}$ will be underestimated using Eq. (2), given that $F_{f,1} = f(\overline{U}^2)$. This assumes the approach taken in [7], where the depth averaged flow is used to calculate the force on a turbine (or fence in this case) using Eq. (2), and that the force on a fence is related to flow at hub height (mid depth) only. This error is quantified in Section 4 by comparing the estimated array drag from the experiment obtained from load cell measurement on each porous fence with results from Eq. (2).

Fig. 6 shows the ambient centreline streamwise, transverse and vertical turbulence intensity distribution in the vertical plane using Case A: without roughness and Case B: with roughness, using Eq. (9), where U_i is the mean velocity and u_i' is the fluctuating velocity component where $i = x, y, z$, correspond to the longitudinal, lateral and vertical directions respectively.

Results for flow using Case A: without roughness agree within 5% of measurements taken at Nodule Point, Admiralty Head [40] and the Sound of Islay [41] in the lower 20% of the water column.

$$I_i = 100\sqrt{\frac{\langle u_i'^2 \rangle}{U_i^2}} \tag{9}$$

Maximum recorded flow velocities of 1.8 m/s at z/h = 0.2 and 3.2 m/s at z/h = 0.14 were obtained at Nodule Point and Admiralty Head respectively whilst in the Sound of Islay the mean flow reached 2.5 m/s at z/h = 0.1. Transverse and vertical turbulence intensities compare less well, with [41] observing approximately 9–10% and 7–8% turbulence intensities in the transverse and vertical directions respectively, giving a ratio of streamwise turbulence intensity to transverse and vertical

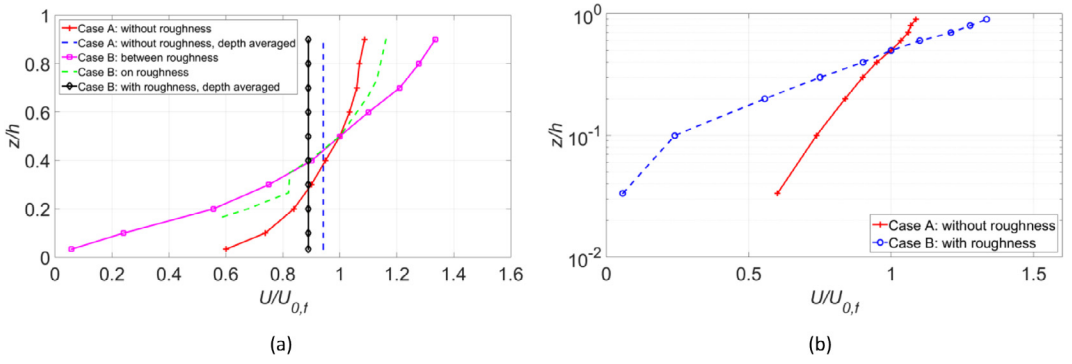

Fig. 5. Vertical distribution of ambient streamwise flow for flow using Case A: without roughness and Case B: with roughness with depth averaged flow velocity, $\overline{U}$ to demonstrate the discrepancy between $\overline{U}$ and U_f. (b) Logarithmic distribution in ambient streamwise flow using Case A: without roughness and Case B: with roughness. Results are normalised by the mid depth flow velocity, $U_{0,f}$.

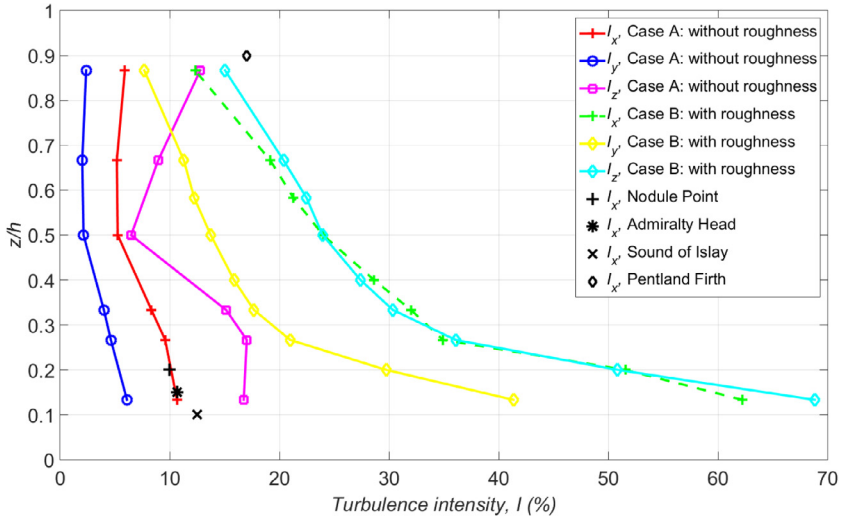

Fig. 6. Vertical distribution of ambient streamwise (x), transverse (y) and vertical (z) turbulence intensity using Case A: without roughness and Case B: with roughness obtained experimentally from ADV measurements.

intensities of 1:0.75:0.56 for the Sound of Islay. Flume measurements give the same ratio as 1:0.57:1.57, showing significantly higher turbulence intensity in the vertical relative to the streamwise and transverse directions.

Case B: with roughness significantly enhanced turbulence intensity in the streamwise, transverse and longitudinal directions. Eddies shed off the leading edge of each roughness strip increased turbulence intensity to enhance mixing between the flow in the roughness layer and the outer flow, augmenting momentum exchange [33]. This was found in [42], where energetic vortices shed by pronounced ripples over a rough surface enhanced vertical transfer of momentum. Values observed here are more representative of higher energy sites such as the Pentland Firth, where streamwise turbulence intensities of 17% were recorded close to the free surface [43].

ADV measurements were taken at 0.1 m intervals laterally across the flume at height $z/h = 0.5$ to quantify the extent to which the lateral boundary layer from each of the flume side walls effects centreline measurements. Both Case A: without roughness and Case B: with roughness demonstrated a relatively flat lateral flow profile across the flume. The boundary layer on either side wall extends no further than 0.15 m laterally towards the centreline so does not encroach on centreline measurements.

Table 2 shows experimental results used to estimate the ambient bed drag, $F_{b,0}$ from Eq. (1) using Case A: without roughness and Case B: with roughness. Bed drag $F_{b,0}$ using Case A: without roughness was very low; within the same order as the precision of depth measurements h_i and h_o (±1 mm) making $F_{b,0}$ highly sensitive to the magnitude of the resultant hydrostatic force $F_i - F_o$. Case B: with roughness increases bed drag significantly as would be expected.

4.2. Single fence

Observations of wake flow downstream of a single fence using Case A: without roughness (Fig. 7a) demonstrate that momentum transfer between the wake and bypass flow above and below the fence was insufficient to recover the flow downstream of the fence, where at a distance of $18l_z$ downstream of the fence, $U_f = 0.82U_{0,f}$. As a consequence of this, additional fence(s) positioned downstream of the first will be subjected to this type of change in incident velocity. Based on previous experimental results of the wake downstream of a porous disk [13] where wakes were shown to persist over twenty diameters downstream, it is highly likely that this will be a feature of full-scale arrays, as has been shown to be the case from full scale windfarm measurements [19].

For Case B: with roughness, higher ambient turbulence intensity enhanced momentum transfer between the wake and bypass flow to improve near wake recovery in comparison with flow over Case A: without roughness. This is shown in

Table 2
Experimental measurements of inlet depth h_i taken at $x = 5$ m, outlet depth h_o taken at $x = 13$ m, depth averaged inlet and outlet flow velocity U_i and U_o, hydrostatic forces F_i and F_o, the weight component F_w and bed drag force F_b using the force balance described by Eq. (1).

Roughness case	h_i (m)	h_o (m)	U_i (m/s)	U_o (m/s)	F_i (N)	F_o (N)	$F_w sin\theta$ (N)	$F_{b,0}$ (N)
A: without roughness	0.295	0.310	0.249	0.237	585	646	63	2
B: with roughness	0.289	0.301	0.223	0.209	559	607	61	14

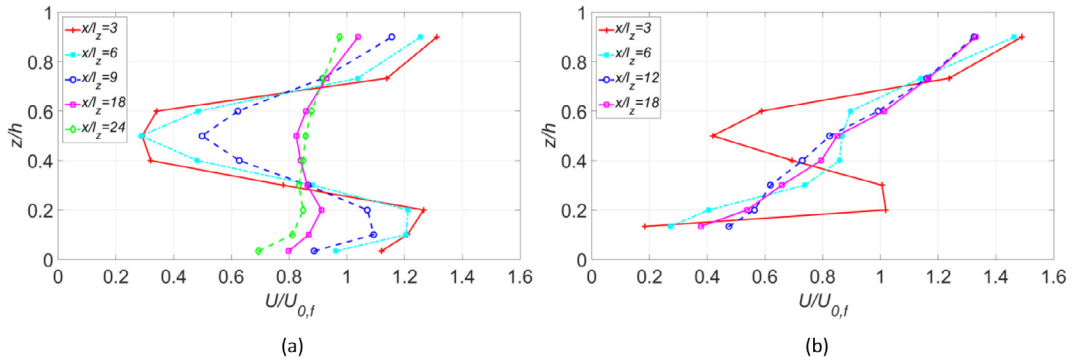

Fig. 7. Vertical flow distribution at positions downstream of a single fence positioned perpendicular to the flow using (a) Case A: without roughness (b) Case B: with roughness. Results normalised by the hub height flow velocity, $U_{0,f}$ $20l_z$ upstream of the fence.

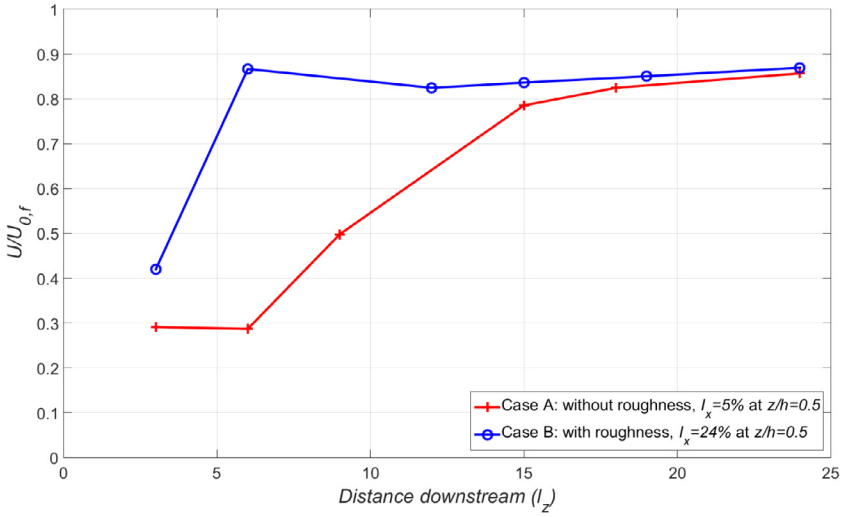

Fig. 8. Mid depth wake recovery downstream of a single fence using Case A: without roughness and Case B: with roughness, normalised by hub height flow velocity, $U_{0,f}$ $20l_z$ upstream of the fence.

Fig. 8, where at a distance of $5l_z$ downstream of the fence the mid depth flow velocity had recovered to approximately the same magnitude as the flow in Case A: without roughness by $18l_z$ downstream. The consequence of this is that for arrays with row spacing $l_f < 15l_z$, the force incident on downstream fences is likely to be higher in comparison with flow in Case A: without roughness, giving a greater total array force, $\overline{F}_a$ from Eq. (2), assuming the same upstream hub height flow velocity, $U_{0,f}$ and number of fences n.

In the far wake where $x > 20l_z$, flow using Case A: without roughness and Case B: with roughness converge to a similar value of flow velocity within 5%, giving $U_f = 0.87U_{0,f}$. Therefore when $x > 20l_z$ the wakes are independent of ambient turbulence intensity (Fig. 8). Coincidentally the far wake deficit shown in Fig. 8 is approximately the same magnitude as the difference between ambient depth averaged flow velocity $\overline{U}$ and ambient flow velocity at porous fence centroid height $U_{f,0}$ shown in Fig. 7. This may improve the accuracy of the depth averaged formulation of array drag given by Eq. (2) when modelling a multi row array (as opposed to a single isolated fence) because depth averaged flow velocity $\overline{U}$ becomes a better representation of flow velocity in the far wake of a porous fence U_f where the next downstream fence is positioned.

The thrust coefficient of a single fence, C_t remained approximately constant with upstream flow velocity, $U_{0,f}$ for flow over Case A: without roughness (Fig. 9). In contrast C_t reduced significantly for flow over Case B: with roughness with increasing upstream flow velocity, both when the fence was positioned half way between roughness strips and directly above a roughness strip in more constrained flow. This is likely to be related to the eddies shed off the roughness, which are a function of $U_{0,f}$. For Case B: with roughness, the fence positioned directly above the roughness strip experiences an initial increase in thrust coefficient C_t with increased upstream flow velocity $U_{0,f}$. The cause of this is unclear, however it is likely that it also relates to the Reynolds number dependency of eddies shed off the roughness strips upstream of the fence and/or the local blockage effect caused by the alignment of the porous fence with the roughness strip. For the purposes of these experiments

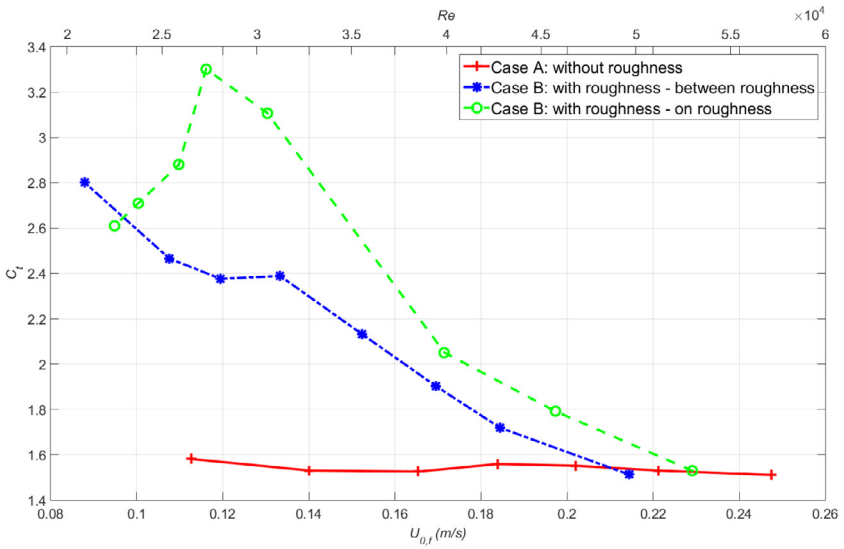

Fig. 9. Variation in thrust coefficient, C_t of a single fence with upstream Reynolds number (using hydraulic radius as the characteristic length scale and $U_{0,f}$ as the characteristic velocity scale) using Case A: without roughness and Case B: with roughness. Upstream flow velocity $U_{0,f}$ is plotted on the second x axis.

the flow incident on porous fences within the porous fence arrays remains greater than $U_{0,f} > 0.15$ m/s, so this low velocity region was not investigated further. For Case B: with roughness, with $U_{0,f} > 0.15$ m/s the thrust coefficient C_t reduced linearly with $U_{0,f}$. For numerical estimates of array drag in Section 4.4, an average linear relationship between flow and C_t was used based on $\overline{U} > 0.15$ m/s, giving a linear decrease in C_t with increasing Reynolds number for $Re > 4 \times 10^4$:

$$C_t = 3.5 - \frac{Re}{2.5 \times 10^4} \tag{10}$$

4.3. Array flow characterisation

Fig. 10a shows the flow distribution in the vertical plane $6l_z$ downstream of fences 1–5 using Case A: without roughness with array 7 ($\lambda = 0.155$, $l_f = 7l_z$). Out of all fences in the array, flow at centroid height ($z/h = 0.5$) through Fence 1, $U_{f,1}$ was highest as it was not in the wake of any upstream fences, so was positioned in ambient flow. As a result the reduction in flow momentum through Fence 1 was also greatest, creating a high wake flow deficit directly downstream of the fence so that the flow velocity at mid depth hitting Fence 2 was significantly reduced (i.e. $U_{f,2} < U_{f,1}$). The bypass flow above and below the fence bottom edge where $z/h < 0.33$ and $z/h > 0.66$ respectively increased to satisfy continuity.

In the region between Fence 1 and 3, the flow was transitioning to an equilibrium state where the drag from fences and the bed is in balance with the longitudinal pressure gradient and weight component that drives flow through the array, as described by Eq. (1). In this transition region at Fence 2 using array 7 ($\lambda = 0.155$, $l_f = 7l_z$) the depth averaged flow, $\overline{U}/U_{0,f}$ was approximately 180% greater than the mid depth flow velocity, $U_f/U_{0,f}$ because of the presence of the wake from Fence 1. This would incur a significant error in the depth averaged force attributed to Fence 2 in a depth averaged drag formulation such as Eq. (2) using high density porous fence arrays. For array 7 this is also true in the equilibrium region downstream of Fence 3, where the depth averaged flow velocity $\overline{U}$ overpredicts the flow velocity through each porousfence at $z/h = 0.5$ by 25%.

By Fence 3 the flow reached an equilibrium described by Eq. (1) where the opposing forces on the flow (the thrust on Fence n, $F_n = f(C_t, \overline{U}^2, A_t)$ and bed drag, $F_b = f(\overline{U}^2, \lambda, z_0)$) were closely balanced against the longitudinal pressure gradient and weight component, F_w driving the flow so that the wake downstream of successive fences recovers to approximately the same magnitude, $U_{f,n}$.

By Fence 3 the flow reached an equilibrium described by Eq. (1) where the opposing forces on the flow (the thrust on Fence n, $F_n = f(C_t, \overline{U}^2, A_t)$ and bed drag, $F_b = f(\overline{U}^2, \lambda, z_0)$) were closely balanced against the longitudinal pressure gradient and weight component, F_w driving the flow so that the wake downstream of successive fences recovers to approximately the same magnitude, $U_{f,n}$.

$$U_{f,n} - \sum U_{f,n} < \Delta U \tag{11}$$

For all arrays, equilibrium conditions were reached after three rows (Figs. 10b and 11b), where the flow velocity through each remaining downstream equilibrium fence (downstream of the three transition fences) was within ±2.5% of the flow speed through the final fence. This is referred to as the equilibrium flow velocity, $U_{f,\infty}$ from now on.

For each array the highest flow was through Fence 1, $U_{f,1}$ as it was not obstructed by upstream fences (Fig. 10b). Downstream of Fence 1 the greatest velocity deficit occurs, so that the lowest flow is through Fence 2, $U_{f,2}$. The wake deficit downstream of Fence 1 is most noticeable for high array density cases where row spacing l_f is small, reducing the longitudinal distance available for wake recovery. To limit the reduction in drag and therefore increase the generated power from row 2, it would be beneficial to increase the row spacing between Fence 1 and 2, with further rows added with gradually reduced row spacing. This was not investigated further here but is the subject of ongoing work.

Since the wake flow is not modelled in depth averaged numerical models (as shown in Fig. 2), the distributed drag approach cannot be expected to accurately predict the drag on fences within the transition region when an uneven distribution in drag between fences occurs. However, analysis of load cell measurements on each fence shows that the average force on fences within the transition region (Fences 1–3) (Eq. (12)) is within 10% of the average force on each fence in the equilibrium region (Fence 4 onwards) (Eq. (13)) and within 5% of the average force on each fence in the whole array (Eq. (14)) over all array densities (Table 3). Therefore, even within the transition zone where there is a highly uneven distribution of drag amongst the first three fences, the average force amongst porous fences within this region was still representative of the total array average.

$$\overline{F}_{trans} = \frac{1}{3}\sum_{i=1}^{3} F_{f,i} \tag{12}$$

$$\overline{F}_{eq} = \frac{1}{n-3}\sum_{i=4}^{n} F_{f,i} \tag{13}$$

$$\overline{F}_{array} = \frac{1}{n}\sum_{i=1}^{n} F_{f,i} \tag{14}$$

The magnitude of $U_{f,\infty}$ increased with increased row spacing, l_f (reduced array density, λ) for Case A: without roughness and Case B: with roughness as shown in Figs. 10b and 11b respectively due to greater wake recovery between fences. $U_{f,\infty}$ also increases with increased ambient turbulence intensity (for flow over Case B: with roughness), which enhanced mixing between the wake and bypass flow hence improving wake recovery, as has been shown experimentally by Blackmore et al. [44] and Mycek et al. using prototype turbines [45,46] (Figs. 11b and 12). The magnitude of $U_{f,\infty}$ was also effected by other features such as fence drag coefficient, C_t and ambient turbulent length scales, however these were not varied in the experiments due to time constraints.

For lower array densities and/or higher ambient turbulence intensity, the difference between $U_{f,1}$,$U_{f,2}$ and $U_{f,3}$ in the transition zone was less pronounced because of greater wake recovery (Figs. 10b and 11b). For Case B: with roughness, the flow recovered to approximately the same magnitude by the point it reached each successive fence, hence removing the transition zone completely so that the flow incident on each fence was equal (Fig. 11b). This resulted in an even distribution in drag amongst all fences apart from Fence 1 which was out of the wake of upstream fences.

Fig. 12 shows that for high ambient turbulence intensity flow using Case B: with roughness, there was a 6% reduction in equilibrium velocity $U_{f,\infty}$ as array density was increased from $\lambda = 0.07$ to $\lambda = 0.16$. Over the same array density range, porous fence arrays in the lower ambient intensity flow using Case A: without roughness gave a 23% reduction in equilibrium velocity $U_{f,\infty}$. To determine whether it is beneficial to add an additional row to a marine current turbine array in a pre-defined plot area, the power generated by the added row must be greater than the reduction in power generated by the existing rows due to the reduction in equilibrium flow velocity with increased array density. This can only be understood with site specific array optimisation given that wake recovery is dependent on ambient turbulence intensity.

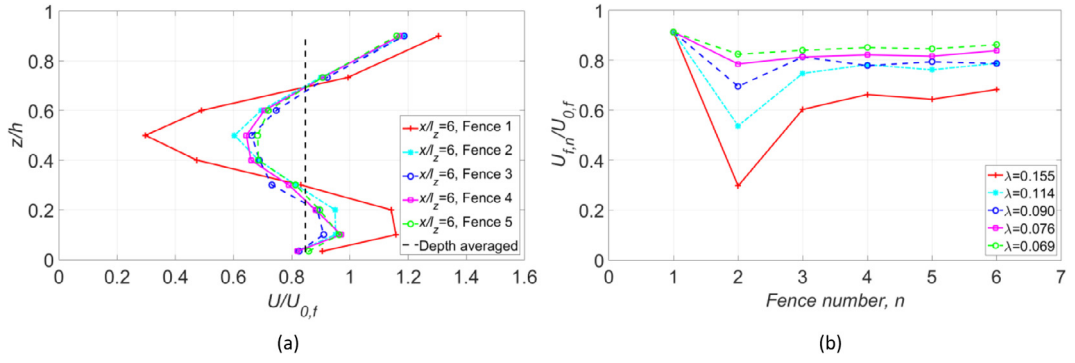

Fig. 10. (a) Vertical flow distribution $1l_z$ upstream of fences n = 1, 2, 3, 4, 5, using array 7 ($\lambda = 0.155$, $x_f = 7l_z$) with Case A: without roughness, (b) mid depth flow through successive fences for all 5 arrays using Case A: without roughness. All results normalised by the mid depth flow velocity, $U_{0,f}$ $20l_z$ upstream of Fence 1.

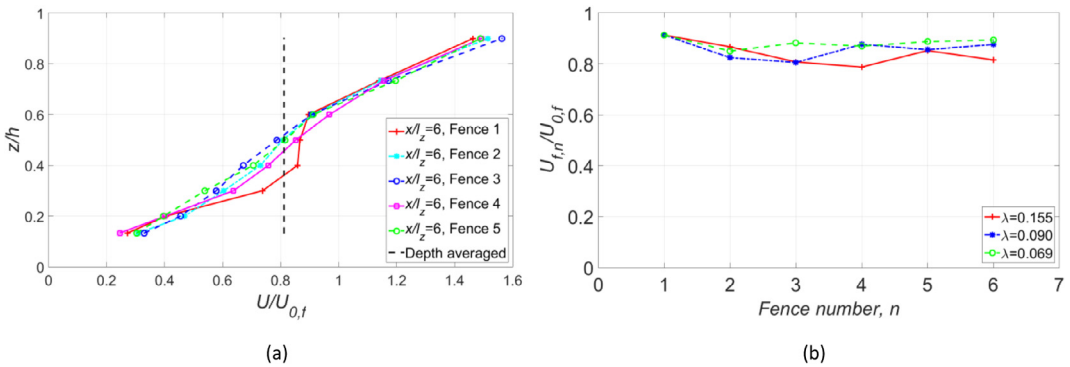

Fig. 11. (a) Vertical flow distribution $6l_z$ upstream of fences 1, 2, 3, 4, 5 using array 7 ($\lambda = 0.155$, $l_f = 7l_z$) with Case B: with roughness, (b) mid depth flow through successive fences for all 5 arrays using Case B: with roughness. All results normalised by the hub height flow velocity,$U_{0,f}$ $20l_z$ upstream of the fence.

Table 3
Average force amongst fences in the transition region (Eq. (12)), equilibrium region (Eq. (13)) and whole array (Eq. (14)) for arrays using Case A: without roughness.

λ	$\overline{F}_{trans}$	$\overline{F}_{eq}$	$\overline{F}_{array}$
0.069	5.69	5.44	5.57
0.076	5.22	5.00	5.10
0.090	4.93	4.59	4.73
0.114	4.89	4.47	4.63
0.155	4.24	4.17	4.19

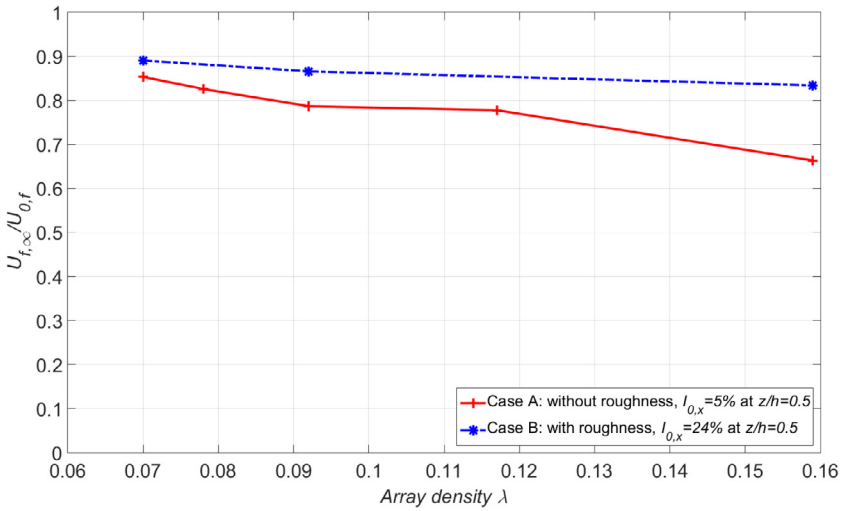

Fig. 12. Variation in equilibrium flow velocity $U_{f,\infty}$ with array density and ambient turbulence intensity using Case A: without roughness and Case B: with roughness. Results normalised by upstream mid depth flow velocity $U_{0,f}$.

4.4. Force balance

Ultrasonic distance measurements along the centreline of the flume show that flow depth upstream of any given array was less than the flow depth downstream so that depth increased across the array. Since the flume bed elevation drops approximately linearly with distance downstream of the inlet ($S_0 = 0.0015$), free surface elevation also dropped across the arrays. As fences were added, the total array drag opposing the flow increased. This resulted in an increase in upstream depth with array density, whilst downstream depth was independent of array density so remained constant for all cases. This led to an increase in the hydrostatic force driving flow in the *x* direction with increasing array density, λ to counter the increase in

array drag, F_a. Results from the force balance (Eq. (1)) are shown in Tables 4 and 5 for Case A: without roughness and Case B: with roughness respectively. For Case A: without roughness, the estimated bed drag was very low, as was the case for the ambient flow regime in Section 4.1. This is supported by estimates of skin friction based on empirical formulations for turbulent flow over flat plates such as Eq. (15) [47], where Re_L is the Reynolds number of the flow using the flume length as the characteristic length. Calculations confirm that bed drag F_b is less than 5% of the resultant hydrostatic force $(F_i - F_o)$, the weight component force $F_w sin\theta$ and the array force F_a for all cases listed in Table 4. In some cases, $F_b < 0$ which is physically incorrect. Given that F_b was so close to zero in all cases and highly sensitive to small error in inlet and outlet depth measurements h_i and h_o, it is thought that this is the reason for this inconsistency.

$$C_b = \frac{0.074}{Re_L^{1/5}} \tag{15}$$

In Fig. 12 empirical array drag is plotted using the array drag coefficient, $C_{t,a}$, defined as:

$$C_{t,a} = \frac{F_a}{\frac{1}{2}\rho|\overline{U}|\overline{U}A_a} \tag{16}$$

where A_a is the total frontal area of all fences in the array and F_a is the array force obtained from load cell measurements. This was compared with a numerical estimate for array drag coefficient using Eq. (2) with C_t obtained from the performance of an individual fence (Fig. 9) as is commonly done in literature for individual turbines [7,8]. For Case A: without roughness, $C_{t,a} = 1.54$ was used. For Case B: with roughness, $C_{t,a}$ was defined using Eq. (10).

For Case A: without roughness numerical array drag coefficient was predicted within 10% of experimental results for array density, $\lambda < 0.07$ (Fig. 13). This is in part due to the fact that depth averaged flow velocity underestimates the mid-depth flow (Fig. 5), so that within the array where fence flow reduces due to upstream wakes (as was seen downstream of a single fence in Fig. 8), a depth averaged flow velocity becomes a reasonable representation of the flow through each fence. In the region where $\lambda < 0.07$, increasing array density gives a linear increase in array drag. As array density exceeds this value, numerical array drag starts to overestimate experimental results. This is caused by the slow moving wake from upstream fences which impedes on downstream fences, reducing the equilibrium flow velocity, so hence reducing fence drag. Depth averaged flow velocity does not account for this so that $\overline{U} > U_f$, as was shown in Fig. 10a for array case 7.

For Case B: with roughness (Fig. 13) experimental and numerical results agreed within 10% over the whole array density range. This was due to enhanced wake recovery as a result of augmented ambient turbulence intensity in the near wake as was shown in Fig. 8 for the wake downstream of a single porous fence. In this case wake flow impeded less on downstream fences so that $\overline{U} \approx U_f$, as was seen in Fig. 11a for array case 7. Under these conditions there is an even distribution in drag over all fences, eliminating the transition region at the front of the arrays (Fig. 11b) with the exception of Fence 1.

A depth averaged numerical estimate for effective array drag coefficient, C_e was calculated using Eq. (5) for all array cases. Results for C_e were then compared with experimental data, where $C_e = \frac{1}{2}\lambda C_{t,a}$ and $C_{t,a}$ is the array thrust coefficient plotted in Fig. 13 using Eq. (15). Results (Fig. 14) show the same trend as in Fig. 13 where for Case A: without roughness and array density $\lambda < 0.07$, estimated numerical array drag using Eqs. (2) and (5) agreed within 7% of experimental results. Any further increase in λ resulted in an error exceeding 10%, where numerical array drag was overestimated because the depth averaged flow, $\overline{U}$ within the array does not account for the variation in flow velocity in the vertical plane caused by fence wake, so that $\overline{U} > U_f$.

For flow using Case B: with roughness (Fig. 14) reasonable agreement between experimental and numerical results within 5% was observed for all array densities with the exception of $\lambda = 0.07$. This is thanks in part to the depth averaged approach, which for ambient logarithmic boundary layer flow under-predicts the flow velocity at fence centroid height, as was shown in Fig. 5a. Since in the arrays wakes impede on downstream porous fences hence reducing the flow velocity through each fence, the depth averaged flow speed becomes a closer representation of fence flow velocity inside the arrays when array density $\lambda < 0.07$. Since depth averaged flow velocity $\overline{U}$ is used in Eq. (2) to estimate array drag numerically, this gives better agreement with load cell measurements obtained experimentally. Nevertheless the parameterisation of array drag described by Eq. (2) appears to be robust within the realistic array density range of $\lambda < 0.07$, which corresponds to a

Table 4
Experimental measurements with Case A: without roughness of inlet depth h_i taken at $x = 5$ m, outlet depth h_o taken at $x = 13$ m, depth averaged inlet and outlet flow velocity U_i and U_o, hydrostatic forces F_i and F_o, the weight component F_w, array force F_a and bed drag force F_b using a force balance (Eq. (1)).

Case	λ	h_i (m)	h_o (m)	$\overline{U}_i$ (m/s)	$\overline{U}_i$ (m/s)	F_i (N)	F_o (N)	$F_w sin\theta$ (N)	F_a (N)	F_b (N)
1	→0	0.295	0.310	0.242	0.231	585	646	63	6	~0
2	0.032	0.297	0.310	0.242	0.231	593	646	63	12	~0
3	0.069	0.299	0.310	0.228	0.220	601	646	63	22	~0
4	0.076	0.301	0.310	0.235	0.229	609	644	64	25	~0
5	0.090	0.303	0.311	0.238	0.232	615	648	64	29	~0
6	0.114	0.303	0.310	0.248	0.242	617	646	64	33	~0
7	0.155	0.305	0.310	0.235	0.232	625	646	64	46	~0

Table 5
Experimental measurements with Case B: with roughness of inlet depth h_i taken at x = 5 m, outlet depth h_o taken at x = 13 m, depth averaged inlet and outlet flow velocity U_i and U_o, hydrostatic forces F_i and F_o, the weight component F_w, array force F_a and bed drag force F_b using a force balance (Eq. (1)).

Case	λ	h_i (m)	h_o (m)	$\overline{U}_i$ (m/s)	$\overline{U}_o$ (m/s)	F_i (N)	F_o (N)	$F_w sin\theta$ (N)	F_a (N)	F_b (N)
1	→0	0.290	0.300	0.234	0.226	565	605	61	6	16
2	0.032	0.292	0.300	0.228	0.222	573	605	62	11	19
3	0.069	0.295	0.300	0.226	0.222	583	605	62	19	21
4	0.076	0.296	0.300	0.219	0.216	587	605	62	24	20
5	0.090	0.297	0.301	0.239	0.236	593	609	62	32	14
6	0.114	0.298	0.300	0.212	0.210	595	605	62	32	21
7	0.155	0.296	0.295	0.212	0.213	589	585	62	49	16

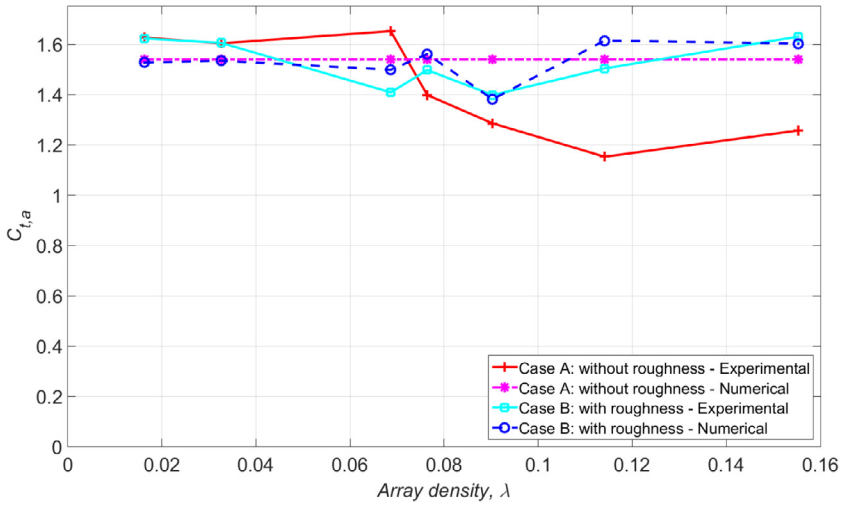

Fig. 13. Variation in total array drag coefficient, $C_{t,a}$ with array density using Case A: without roughness and Case B: with roughness. Experimental and numerical expression for $C_{t,a}$ given by Eq. (10) and Section 4.2 respectively.

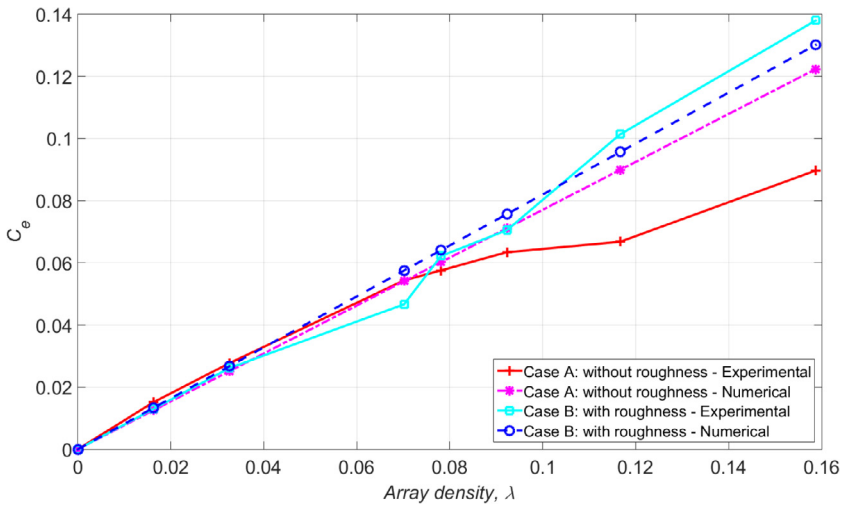

Fig. 14. Experimental and numerical variation in effective array drag coefficient, C_e for all arrays using Case A: without roughness and Case B: with roughness.

lateral and longitudinal spacing between turbines of just 1 and 5.5 diameters respectively (excluding support structure drag). Caution should be taken when the inflow is not logarithmic, and when porous fences/disks/turbines are positioned at different heights, as this will alter the level of agreement between the depth averaged flow velocity and the flow velocity through the centroid height of the fence/disk/turbine.

Importantly, the change in depth between the porous array inlet and outlet results in a change in depth averaged flow velocity through the array. In the most extreme case of array 1 using Case A: without roughness, there is a 3.5% change in $\overline{U}$, which is significant for approximations of numerical array drag, C_e as already discussed. This was accounted for by averaging $\overline{U}$ over array length by assuming a linear free surface elevation drop across each array. This assumption has been verified using the backwater curves method [48] and a simple 2D numerical model that simulates the linear rate of change of free surface elevation over a distributed drag for flow in an open channel with the same input parameters as the experiment.

4.5. Bed drag

Experimental results from Tables 2 and 5 were used with the force balance described by Eq. (1) to estimate the change in bed drag opposing the flow as a result of the presence of arrays ($F_b - F_{b,0}$). Results obtained for Case A: without roughness were not used in this analysis as bed drag was very low, causing some unphysical cases where $F_b < 0$, as discussed in Section 4.4. Results for Case B: with roughness show that over the realistic array density range ($\lambda < 0.07$), increasing array density increases bed drag coefficient C_b significantly (Fig. 15), where by porous array case 3 ($\lambda = 0.07$) the new bed drag coefficient C_b was 150% of the ambient bed drag coefficient $C_{b,0}$.

The added bed drag coefficient $C_{b+} = C_b - C_{b,0}$ due to the presence of the porous fence arrays was a significant proportion of the ambient bed drag coefficient $C_{b,0}$, especially at high array density where for $\lambda > 0.07$, C_{b+} was of the same magnitude as $C_{b,0}$ (Fig. 15). Added bed drag coefficient C_{b+} was also a significant proportion of array drag coefficient C_e, especially at low array density when C_e was low relative to the ambient bed drag $C_{b,0}$ (Fig. 15). The error in total added drag (due to the presence of porous fence arrays) incurred by not accounting for the increase in bed drag C_{b+} ranged between 10 and 20% over the porous fence array densities used. The greatest error in total added drag coefficient was for low array densities, where the added bed drag coefficient $C_{b+} = C_b - C_{b,0}$ was a higher proportion of the total added bed drag coefficient $C_b + C_e$. For array density $\lambda < 0.1$, the error in total added bed drag $C_b + C_e$ was between 10 and 20%, which reduced to 9% for $\lambda = 0.159$.

As a consequence neglecting the added bed drag $C_{b+} = C_b - C_{b,0}$ will lead to array drag being underestimated by up to 20%. Since for these experiments the roughness strip height $k = 0.03$ m was 10% of the flow depth $h = 0.3$ m, this is representative of a very rough bed. Therefore it is expected that the 20% error in total added drag coefficient is an upper bound for the error incurred by neglecting the increase in bed drag caused by the presence of an array. Neglecting this effect in regional scale hydrodynamic model simulations will lead to a misrepresentation of the flow dynamics surrounding an array, where a reduced array drag is likely to lead to reduced flow diversion around the array and a reduction in array wake length, two important features for determining array-array spacing and interaction.

The added bed drag coefficient C_{b+} is attributed in part to an increase in bed shear in the bottom third of the water column directly below the bottom edge of each fence ($z/h < 0.33$) close to the bed. Fig. 16 shows the difference in spatially averaged shear profile $u'w'$ for porous fence array case 7 ($\lambda = 0.159$, $l_f = 7l_z$), 5 ($\lambda = 0.092$, $l_f = 13l_z$) and 3 ($\lambda = 0.070$, $l_f = 19l_z$) for both Case A: without roughness and Case B: with roughness where the profiles are an average of measurements between each equilibrium (out of the transition region). For both roughness cases as array density increased, the spatially averaged shear

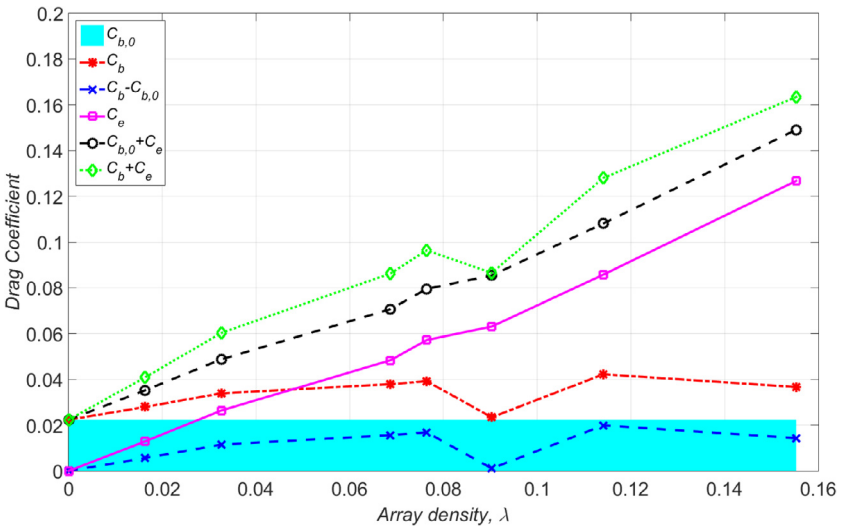

Fig. 15. Change in bed drag C_b, array drag C_e, total drag coefficient $C_b + C_e$, added bed drag coefficient $C_b - C_{b,0}$, total added drag coefficient $C_{b,0} + C_e$ (neglecting change in bed drag) and total added drag coefficient $C_b + C_e$ as a result of increasing array density using Case B: with roughness. Ambient bed drag coefficient $C_{b,0}$ is also shown for comparison.

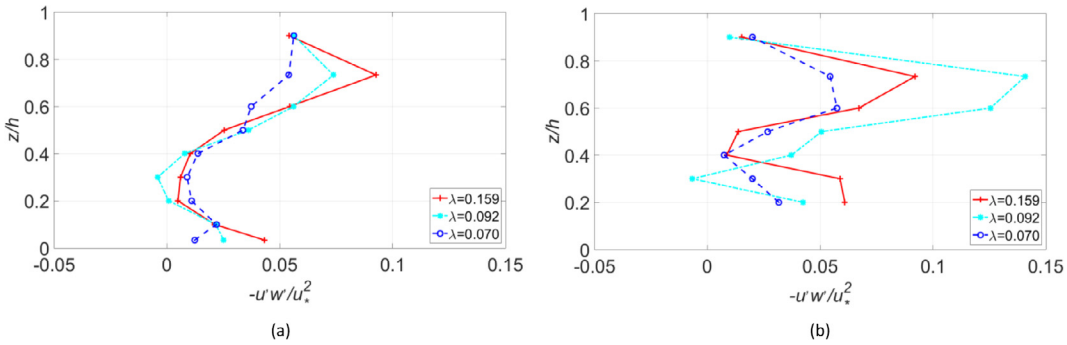

Fig. 16. Vertical distribution of shear stress $u'w'$ downstream of equilibrium fences using (a) Case A: without roughness and (b) Case B: with roughness. Results are normalised by ambient friction velocity squared.

stress $u'w'$ directly below the fence and close to the bed ($z/h < 0.33$) also increased, which is commonly used to estimate bed drag [49].

The presence of the roughness strips reduced the open area under each fence, causing greater flow acceleration in this region compared to flows over Case A: without roughness. The interaction between this accelerated flow and the frontal area of each roughness strip increased the contribution of bed form drag opposing the flow (also called pressure drag) given by the difference in pressure between the front and back faces of each roughness element. Large Eddy Simulations (LES) of flow over k-type roughness show that pressure drag is significantly greater than the frictional drag component acting on a roughness surface, where recirculation downstream of each roughness element causes the frictional drag to act in the flow direction [33]. Form drag was less significant using Case A: without roughness as the frontal face of the roughness is significantly smaller, so protrudes far less into the oncoming flow.

For Case B: with roughness measurements of shear stress directly above the roughness strips at $z/h = 0.133$ varied greatly, where roughness strips come up to $z/h = 0.1$. This is likely to be because of the highly complex flow close to the roughness strips, where separation and reattachment occurs between adjacent roughness strips, throwing large eddies out into the outer flow [33], causing a local maximum in shear stress. Given that ADV measurements were obtained at different longitudinal positions relative to the roughness strips between each fence (some in closer proximity to the roughness strips than others depending on the phasing of roughness strips to fences), high variability in shear stress was observed. For this reason $u'w'$ at $z/h = 0.133$ was discarded in Fig. 16b.

As an aside, Fig. 16 shows a region of high shear above the fence top edge height ($z/h = 0.75$) where the slow moving wake meets the fast moving bypass flow. At high array density the spatially averaged shear at this height is relatively high because there are many fences causing this interaction. To reduce array density the number of fences n within the plot area was reduced, causing this interaction to occur less frequently, resulting in a reduction in spatially averaged shear stress between the upper wake and bypass flow. For Case B: with roughness array case 5 needs repeating as unexpectedly it does not follow this trend (Fig. 15b). This could be the consequence of Reynolds number as upstream flow velocity was slightly higher in this case.

Results indicate that when modelling arrays, the added bed drag C_{b+} must be accounted for, otherwise the total drag $C_b + C_e$ in Eq. (6) will be underestimated. This will reduce the impact the array has on the flow dynamics in terms of flow reduction inside the array, making it likely that extracted array power will be overestimated. Results in Fig. 15 show the error in total added drag coefficient ($C_b + C_e$) could be as high as 20% for very rough beds when form drag is significant as was seen for Case B: with roughness used here. For smoother beds (with lower z_0 and u_*) this error is likely to reduce because the bed drag is a smaller proportion of the overall drag ($C_b + C_e$), as was seen for Case A: without roughness, so any change in bed drag C_{b+} will have a less significant effect.

Further work is required to confirm these relationships given the scattered nature of some data points, such as the decrease in bed drag coefficient for array case 5 ($\lambda = 0.092$) shown in Fig. 15, which could be linked to the drop in array drag coefficient shown in Fig. 13. Work is ongoing to develop a better physical grounding based also on the hydrodynamic characteristics of the bed (z_0), the vertical spacing between the bed and the turbine rotor and the ambient inflow conditions.

5. Conclusions

Flume experiments have been conducted using porous fence arrays to simulate the wakes downstream of densely packed marine current turbine rows. Results of fence load, free surface elevation drop and velocity distribution within each array were used to quantify the accuracy of the distributed drag parameterisation of array drag typically implemented in regional scale models. For logarithmic boundary layers such as the ones considered here, the flow speed at height $z/h = 0.4$ is equal to the depth averaged flow velocity $\overline{U}$. The validity of the distributed drag method relies on agreement between the depth averaged velocity and the velocity at centroid height of the porous fences. In general experimental results for array drag

coefficient using the load cell measurements showed agreement with results from the numerical formulation of array drag (Eq. (2)) within 10% for arrays with density $\lambda < 0.07$. For these lower but more realistic array densities, the depth averaged flow velocity was a reasonable representation of the flow through fences in each array due to wake interaction with downstream fences.

An uneven distribution in drag amongst the first three fences was quantified from load cell measurements, showing the distributed drag method is incapable of quantifying the drag on each individual fence within this transition region. Nevertheless the average force amongst transition fences was in close agreement with fences further downstream, indicating this has no significant impact on the estimate for total array drag.

These results are encouraging given that in reality array density would not be expected to exceed $\lambda = 0.07$, the limit for which experimental results agreed with the numerical formulation of array drag within 10%. This gives confidence in depth averaged resource scale hydrodynamic modelling and the ability of the distributed drag method to accurately model energy extraction from large marine current turbine arrays, which is a useful tool for regulators, developers and investors to develop specific sites.

In comparison to the ambient flow cases, there was an increase in bed drag of up to 95% with the inclusion of porous fence arrays when roughness strips were added to the flume bed. This accounted for an increase in total drag from the bed and the array of up to 20%. The porous fences enhanced flow velocity below fence height, hence increasing the pressure drag acting on the roughness strips. There was no noticeable change in bed drag when using the flume bed in its natural state without roughness strips. Work is ongoing to quantify the relationship between roughness geometry and the change in bed drag caused by porous fence arrays.

Acknowledgements

This work is part of the activities of the Energy and Climate Change Division and the Sustainable Energy Research Group at the University of Southampton (www.energy.soton.ac.uk). It is also supported by ESPRC under the Supergen Marine research programme.

References

[1] T.A. Adcock, S. Draper, T. Nishino, Tidal power generation – a review of hydrodynamic modelling, Proc. Inst. Mech. Eng. Part A 229 (2015) 755–771.
[2] S. Bourban, M. Liddiard, N. Durand, S. Cheeseman, and A. Baldock, High resolution modelling of tidal resources, extraction and interactions around the UK, in 1st Marine Energy Technology Symposium (METS13), 2013, p. 8.
[3] R. Ahmadian, R.A. Falconer, Assessment of array shape of tidal stream turbines on hydro-environmental impacts and power output, Renew. Energy 44 (2012) 318–327.
[4] S. Draper, T.A. Adcock, A.G.L. Borthwick, G.T. Houlsby, Estimate of the tidal stream power resource of the Pentland Firth, Renew. Energy 63 (2014) 650–657.
[5] J. Thiebot, P. Bailly du Bois, S. Guillou, Numerical modeling of the effect of tidal stream turbines on the hydrodynamics and the sediment transport e Application to the Alderney Race (Raz Blanchard), France, vol. 75, pp. 356–365, 2015.
[6] R.A. Walters, M.R. Tarbotton, C.E. Hiles, Estimation of tidal power potential, Renew. Energy 51 (Mar. 2013) 255–262.
[7] D.R. Plew, C.L. Stevens, Numerical modelling of the effect of turbines on currents in a tidal channel – Tory Channel, New Zealand, Renew. Energy 57 (2013) 269–282.
[8] R. Karsten, A. Swan, J. Culina, Assessment of arrays of in-stream tidal turbines in the Bay of Fundy, Proc. R. Soc. A 371 (2012) 189–203.
[9] R.H. Karsten, J.M. McMillan, M.J. Lickley, R.D. Haynes, Assessment of tidal current energy in the Minas Passage, Bay of Fundy, Proc. Inst. Mech. Eng. Part A 222 (5) (Aug. 2008) 493–507.
[10] J. Blanchfield, C. Garrett, A. Rowe, P. Wild, Tidal stream power resource assessment for Masset Sound, Haida Gwaii, Proc. Inst. Mech. Eng. Part A 222 (5) (Aug. 2008) 485–492.
[11] G. Sutherland, M. Foreman, C. Garrett, Tidal current energy assessment for Johnstone Strait, Vancouver Island, Proc. Inst. Mech. Part A 221 (2) (2007) 147–157.
[12] D.S. Coles, L.S. Blunden, A.S. Bahaj, Estimates for the power potential from tidal flows at Alderney Race (Raz Blanchard), Casquets and Big Roussel in the Channel Islands, Proc. R. Soc. A (2016).
[13] L.E. Myers, A.S. Bahaj, Experimental analysis of the flow field around horizontal axis tidal turbines by use of scale mesh disk rotor simulators, Ocean Eng. 37 (2–3) (2010) 218–227.
[14] A.S. Bahaj, A.F. Molland, J.R. Chaplin, W.M.J. Batten, Power and thrust measurements of marine current turbines under various hydrodynamic flow conditions in a cavitation tunnel and a towing tank, Renew. Energy 32 (3) (2007) 407–426.
[15] A. Bahaj, L. Myers, M. Thomson, N. Jorge, Characterising the wake of horizontal axis marine current turbines, in: Proc. 7th EWTEC, 2007.
[16] L.E. Myers, A.S. Bahaj, An experimental investigation simulating flow effects in first generation marine current energy converter arrays, Renew. Energy 37 (1) (Jan. 2012) 28–36.
[17] A.S. Bahaj, L.E. Myers, Shaping array design of marine current energy converters through scaled experimental analysis, Energy 59 (2013) 83–94.
[18] L. Blunden, A. Bahaj, "Tidal energy resource assessment for tidal stream generators, Part A J. Power Energy (2007).
[19] R. Barthelmie, S. Frandsen, L. Jensen, M. Mechali, P.-E. Rethore, Verification of an efficiency model for very large wind turbine clusters, Copenhagen Offshore Wind 2005 Conf., 2005.
[20] L.P. Chamorro, F. Porté-Agel, Turbulent flow inside and above a wind farm: a wind-tunnel study, Energies 4 (11) (2011) 1916–1936.
[21] M.E. Harrison, Comparisons of a large tidal turbine array using the boundary layer and field wake interaction models, in: 2nd International Conference on Ocean Energy (ICOE 2008), 2008, no. October, pp. 1–9.
[22] L.S. Blunden, W.M.J. Batten, M.E. Harrison, A.S. Bahaj, Comparison of boundary-layer and field models for simulation of flow through multiple-row tidal fences, in 8th European Wave and Tidal Energy Conference, 2009, pp. 1–10.
[23] D.S. Coles, L.S. Blunden, A.S. Bahaj, Experimental testing for spatially averaged numerical modelling of large marine current energy converter arrays, in: Asian Wave and Tidal Energy Conference, 2014.
[24] S. Frandsen, On the wind speed reduction in the center of large clusters of wind turbines, J. Wind Eng. Ind. Aerodyn. 39 (1–3) (1992) 251–265.
[25] R. Vennell, S.W. Funke, S. Draper, C. Stevens, T. Divett, Designing large arrays of tidal turbines: A synthesis and review, Renew. Sustain. Energy Rev. 41 (2015) 454–472.

[26] ABPmer, Alderney Regional Environmental Assessment of Renewable Energy: Scoping Report Alderney Commission for Renewable Energy Alderney Regional Environmental Assessment of Renewable Energy: Scoping Report, 2013.
[27] S.G. Haynes, The Effects of Array Installation upon the Morphology of a Headland Associated Linear Sandbank, PhD: Transfer report, 2015, pp. 49–55.
[28] C. Garrett, P. Cummins, The power potential of tidal currents in channels, R. Soc. A 461 (2005) 2563–2572.
[29] D.S. Coles, L.S. Blunden, A.S. Bahaj, The potential for electricity generation using large tidal stream turbine arrays in Alderney Race (Raz Blanchard), Energy (2016).
[30] Jean-Michel Hervouet, Hydrodynamics of Free Surface Flows Modelling With the Finite Element Method, WILEY, 2007, pp. 89–90.
[31] D.J. Moore, Depletion of available wind power by a large network of wind generators, in: 2nd International Conference on Future Energy Concepts, 1979, pp. 302–305.
[32] B. Keogh, L. Myers, A. Bahaj, Tidal stream turbine performance with changes in channel size and geometry, Grand Renew. Energy 2014 (2014) 1–4.
[33] J. Cui, V.C. Patel, C.-L. Lin, Large-eddy simulation of turbulent flow in a channel with rib roughness, Int. J. Heat Fluid Flow 24 (3) (2003) 372–388.
[34] S.F.A. Crespo, J. Hernandez, Survey of modelling methods for wind turbine wakes and wind farms, Wind Energy 24 (1999) 1–24.
[35] R. Cant, I. Castro, P. Walklate, Plane jets impinging on porous walls, Exp. Fluids 32 (2002) 16–26.
[36] A.D. Heathershaw, Comparisons of measured and predicted sediment transport rates in tidal currents, Mar. Geol. 42 (1–4) (1981) 75–104.
[37] A.J. Elliott, The boundary layer character of tidal currents in the Eastern Irish Sea, Estuar. Coast. Shelf Sci. 55 (3) (Sep. 2002) 465–480.
[38] R.W. Sternberg, Friction factors in tidal channels with differing bed roughness, Mar. Geol. 6 (3) (1968) 243–260.
[39] M.R. Raupach, R.A. Antonia, S. Rajagopalan, Rough-wall turbulent boundary layers, Appl. Mech. Rev. 44 (1) (1991) 1.
[40] J. Thomson, B. Polagye, V. Durgesh, M.C. Richmond, Measurements of turbulence at two tidal energy sites in Puget Sound, WA, IEEE J. Ocean. Eng. 37 (3) (2012) 363–374.
[41] I.A. Milne, R.N. Sharma, R.G.J. Flay, S. Bickerton, Characteristics of the turbulence in the flow at a tidal stream power site, Philos. Trans. R. Soc. A (2013).
[42] A.C. Trembanis, L.D. Wright, C.T. Friedrichs, M.O. Green, T. Hume, The effects of spatially complex inner shelf roughness on boundary layer turbulence and current and wave friction: Tairua embayment, New Zealand, Cont. Shelf Res. 24 (13–14) (2004) 1549–1571.
[43] J. Hardwick, I. Ashton, L. Johanning, Field characterisation of currents and near surface eddies in the Pentland Firth, in: 4th Oxford Tidal Energy Workshop, 2015.
[44] T. Blackmore, W.M.J. Batten, A.S. Bahaj, Turbulence generation and its effect in LES approximations of tidal turbines, in: EWTEC 2013, 2013.
[45] P. Mycek, B. Gaurier, G. Germain, G. Pinon, E. Rivoalen, Experimental study of the turbulence intensity effects on marine current turbines behaviour. Part II: two interacting turbines, Renew. Energy 68 (2014) 876–892.
[46] P. Mycek, B. Gaurier, G. Germain, G. Pinon, E. Rivoalen, Experimental study of the turbulence intensity effects on marine current turbines behaviour. Part I: one single turbine, Renew. Energy 66 (2014) 729–746.
[47] Y.A. Cengal, J.M. Cimbala, Fluid Mechanics Fundamentals and Applications, McGraw-Hill, 2006, pp. 426–433.
[48] V. Chow, Open-Channel Hydraulics, McGraw-Hill, New York, 1959.
[49] P.M. Biron, C. Robson, M.F. Lapointe, S.J. Gaskin, Comparing different methods of bed shear stress estimates in simple and complex flow fields, Earth Surf. Process. Landforms 29 (11) (2004) 1403–1415.